IEEE Trans. PAMI, Vol. 31, #3, pp. 385-399, 2009.

Active Polarization Descattering

Tali Treibitz, *IEEE Student Member* and Yoav Y. Schechner, *IEEE Member*

***Abstract*— Imaging in scattering media such as fog and water is important but challenging. Images suffer from poor visibility due to backscattering and signal attenuation. Most prior methods for scene recovery use active illumination scanners (structured and gated), which can be slow and cumbersome. On the other hand, natural illumination is inapplicable to dark environments. The current paper addresses the need for a non-scanning recovery method, that uses active scene irradiance. We study the formation of images under widefield artificial illumination. Based on the formation model, the paper presents an approach for recovering the object signal. It also yields rough information about the 3D scene structure. The approach can work with compact, simple hardware, having active widefield, polychromatic polarized illumination. The camera is fitted with a polarization analyzer. Two frames of the scene are instantly taken, with different states of the analyzer or light-source polarizer. A recovery algorithm follows the acquisition. It allows both the backscatter and the object reflection to be partially polarized. It thus unifies and generalizes prior polarization-based methods, which had assumed exclusive polarization of either of these components. The approach is limited to an effective range, due to image noise and falloff of widefield illumination. Thus, these limits and the noise sensitivity are analyzed. The approach particularly applies underwater. We therefore use the approach to demonstrate recovery of object signals and significant visibility enhancement in underwater field experiments.**

***Index Terms*— Computer vision, Modeling and recovery of physical attributes, Scene Analysis - Color, Physics-based vision, Vision in scattering media, Inverse-problems, Polarization, Image recovery**

I. Introduction

Scattering media exist in bad weather, liquids, biological tissue and even solids [3]. Images taken in scattering media are characterized by loss of contrast. Light passing through undergoes absorption and scattering, causing changes in color and brightness. Moreover, light that is scattered back from the medium along the light of sight (*backscatter*) veils the object, degrading the contrast. Therefore, applying traditional computer vision methods in such environments is difficult. Nevertheless, there is a strong need to perform vision tasks in these media. Examples include vision through biological tissue [16], underwater applications, such as port inspection, measuring ecological systems [15], and navigation in bad weather [1].

Previous studies tackled this challenge in various ways. Some recovered visibility as well as the three dimensional (3D) structure in haze and underwater [38], [39], [40] under distant natural illumination. However, application fields operating in highly turbid media use *artificial illumination* sources at *short* distances, be it underwater or in the human body. However, artificial lighting usually causes a strong *backscatter*. Backscatter can be modulated and then compensated for in image post-processing. Prior modulation methods require acquisition of long image sequences by structured light [21], [23], [31] or time-gating [6], [9], [14], [47], [49]. Ref. [32] required many frames as well, to achieve quality results. Such sequences may lengthen the overall acquisition time. Moreover, such systems may be complex and expensive.

To counter these problems, we look at wide-field (not scanning) illumination with a small (or no) baseline, where the backscatter is modulated by polarization. Preliminary studies [10], [11], [24] indicated that backscatter can be reduced by polarization. However, we go further. By post-processing we remove residual backscatter that is not blocked by optical means. Moreover, a rough estimate of the 3D scene structure may be obtained from the acquired frames. The acquisition setup is a simple modification of instruments used routinely in such media: simply mounting two polarizers, one on the light source and another on the camera. The acquisition process is instantaneous, i.e., requiring only two frames, rather than scanning. In this paper, we describe and demonstrate each step separately.

Some prior methods used polarization in scattering media. Some assumed a negligible degree of polarization (DOP) of the objects [38], [39], [41], [50]. Others assumed the contrary, i.e., that object reflection is significantly polarized, rather than the backscatter [52]. However, here we allow both the backscatter and the object reflection to be partially polarized. Thus, our analysis unifies and generalizes the mentioned previous methods.

The approach is based on several insights into the image formation process. We show that backscatter and attenuation of artificial illumination can be well approximated by simple closed-form parametric expressions. To incorporate polarization, we made some empirical observations in real underwater scenes: in a temperate latitude sea (the Mediterranean), a tropical sea (the Red Sea) and in a murky lake (Sea of Galilee). Our approach has limits stemming from the wide-field nature of the illumination and from the acquisition noise. In this paper, we thoroughly analyze the reconstruction limits of both signal and 3D structure.

In Sec. II, the paper first describes the scientific model of the imaging system, and sets the ground for polarization imaging (Sec. III). The reconstruction is done in two steps: first, we recover the object signal (Sec. IV). Then, we estimate the scene structure (Sec. V). Experimental results follow each step. In Sec. VI we discuss estimation of essential parameters. Then, Sec. VII analyzes the limits of our method due to image noise. Partial results appeared in [50].

II. Statement of the Problem

Consider a perspective underwater camera (Fig. 1). Let $\mathbf{X} = (X, Y, Z)$ be the world coordinates of a point in the water. We set the world system's axes (X, Y) to be parallel to the (x, y) coordinates at the image plane, while Z aligns with the camera's optical axis, and the system's origin is at the camera's center of projection. The projection of $\mathbf{X}$ on the image plane is $\mathbf{x} = (x, y)$.

The authors are with the Dept. of Elect. Eng., Technion - Israel Inst. of Technology, Haifa 32000, Israel.

Email: ttali@tx.technion.ac.il, yoav@ee.technion.ac.il . Phone: +972-4-8294749, Fax: +972-4-8295757.

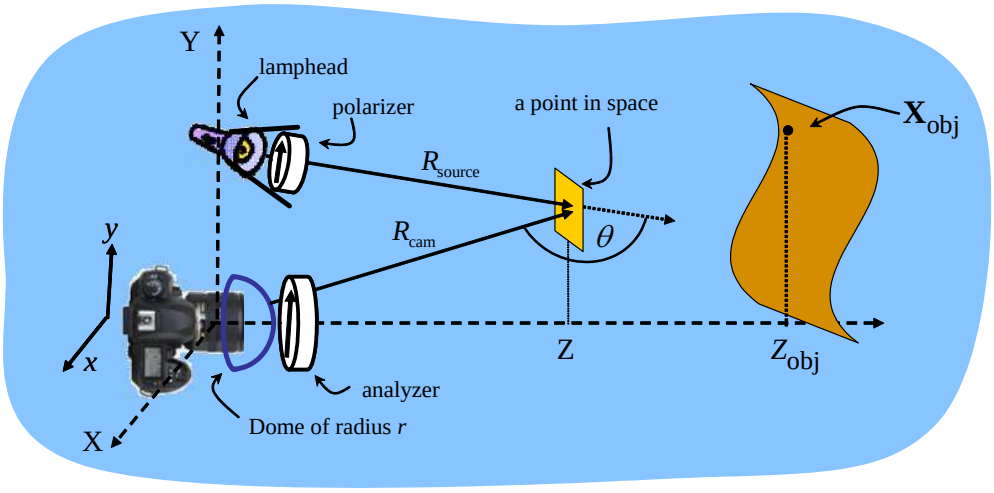

Fig. 1. A camera inside a dome port with a radius r. The variables are detailed in the text.

Fig. 2. Simulation of an underwater scene. The scene was assigned a linearly varying distance map ranging between $[0.2m, 1m]$. (a) A uniformly lit clear scene. (b) The simulated attenuated signal. (c) The backscatter component. (d) The sensed underwater scene, accounting for both scattering and attenuation.

In particular, an object point at $\mathbf{X}_{\text{obj}}$ corresponds to an image point $\mathbf{x}_{\text{obj}}$. The line of sight (LOS) to the object is

$$\text{LOS} \equiv \left\{ \mathbf{X} : \ Z \in [0, Z_{\text{obj}}], \ X = (Z/f)x_{\text{obj}}, \ Y = (Z/f)y_{\text{obj}} \right\}, \tag{1}$$

where f is the camera's focal length. The measured image is

$$I(\mathbf{x}_{\text{obj}}) = S(\mathbf{x}_{\text{obj}}) + B(\mathbf{x}_{\text{obj}}), \tag{2}$$

where $S(\mathbf{x}_{\text{obj}})$ is the object signal and $B(\mathbf{x}_{\text{obj}})$ is the backscatter [17], [26], [28]. Before detailing these components, note that backscatter is the major cause of contrast deterioration [18], rather than signal blur. This was demonstrated in [38], [39] using objective criteria. Interestingly, according to Ref. [53], human vision associates image quality mostly with contrast, rather than resolution. For these reasons, we do not focus here on image blur or deblurring. Rather, we consider the prime effects associated with turbidity to be backscatter and attenuation. Fig. 2 demonstrates these effects.

Define $L_{\text{obj}}(\mathbf{x}_{\text{obj}})$ as the object radiance we would have sensed had no disturbances been caused by the medium along the LOS, and under uniform illumination. Propagation of light to the object and then to the camera via the medium yields an attenuated [17], [26] signal. The signal is

$$S(\mathbf{x}_{\text{obj}}) = L_{\text{obj}}(\mathbf{x}_{\text{obj}}) F(\mathbf{x}_{\text{obj}}), \tag{3}$$

where F is a falloff function described below.

A point $\mathbf{X}$ in the water is at total distance $\|\mathbf{X}\|$ from the camera. If the camera is enclosed in a dome port[1] as in [38], [39], then the distance from the dome to $\mathbf{X}$ is

$$R_{\text{cam}}(\mathbf{X}) = \|\mathbf{X}\| - r, \tag{4}$$

where r is the dome's radius. Consider for a moment a single illumination point source. From this source, light propagates a distance R_{source} to $\mathbf{X}_{\text{obj}}$. Free space propagation creates a $1/R^2_{\text{source}}$ irradiance falloff. Yet, there is turbidity, characterized by an attenuation coefficient c. Hence

$$F(\mathbf{x}_{\text{obj}}) = \frac{\exp\left\{-c\left[R_{\text{source}}(\mathbf{X}_{\text{obj}}) + \|\mathbf{X}_{\text{obj}}\| - r\right]\right\}}{R^2_{\text{source}}(\mathbf{X}_{\text{obj}})} Q(\mathbf{X}_{\text{obj}}). \tag{5}$$

Here $Q(\mathbf{X})$ expresses the non-uniformity of the scene irradiance (Fig. 3), solely due to the angular inhomogeneity of the illumination (anisotropy), which is insensitive to the medium properties. Thus, in water-based media, for example, it can be pre-calibrated in clear water. For multiple illumination sources,

[1]Dome ports often shield cameras from water [38], [39]. With a dome, optical distortions are smaller than when using other shapes of windows, provided that the center of projection of the lens is accurately aligned with the center of the dome. Ref. [38], [39] explains that when the lens and the dome are aligned, the polarization measurement is more accurate because chief light rays do not change their path when passing through the port. Distortions caused by a flat port are analyzed and calibrated in [51].

Fig. 3. An example of an anisotropic illumination pattern $Q(\mathbf{X})$: Even in the same radial distance from the lamphead, the lighting changes laterally.

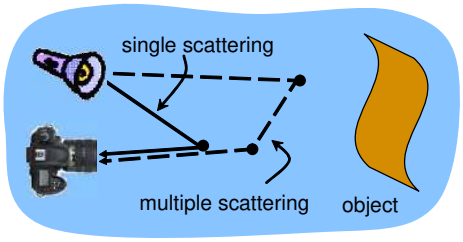

Fig. 4. Backscatter caused by single scattering [solid line] and multiple scattering [dashed].

or for a wide spread source Eq. (5) is derived for each point source, and then all F's are summed up. This can be generalized to include illumination due to multiple scattering [48].

In order to calculate the backscatter that appears in Eq. (2), define first I^{source} as the irradiance of a point in the volume [17] by a small illumination source of intensity L^{source}:

$$I^{\text{source}}(\mathbf{X}) = L^{\text{source}} \left[1/R^2_{\text{source}}(\mathbf{X})\right] \exp[-cR_{\text{source}}(\mathbf{X})]Q(\mathbf{X}). \tag{6}$$

Then, according to the single-scattering model (Fig. 4), the backscatter is given [17], [50] by integration along the LOS

$$B(\mathbf{x}_{\text{obj}}) = \int_{R_{\text{cam}}=0}^{R_{\text{cam}}(\mathbf{X}_{\text{obj}})} b[\theta(\mathbf{X})] I^{\text{source}}(\mathbf{X}) \exp[-cR_{\text{cam}}(\mathbf{X})] dR_{\text{cam}} \ , \quad \mathbf{X} \in \text{LOS}, \tag{7}$$

where $\theta \in [0, \pi]$ is the scattering angle, and b is the scattering coefficient[2] of the medium: it expresses the ability of an infinitesimal medium volume to scatter flux to θ. Eq. (7) applies to each illumination source: accumulating the results yields the total backscatter. Note that the integration in Eq. (7) stops when it reaches the object in the LOS. Therefore, the backscatter accumulates (increases) with the object distance. If there is no object on the LOS, the integration in Eq. (7) continues to an infinite distance. The value of B then increases until it reaches a *saturation value*. We term the distance in which B effectively saturates[3] as the *saturation distance* z_{sat}.

Our goal in this research is two-fold: first, to estimate the backscatter component, in order to remove it from the raw image and reveal the object signal. Second, to study the potential use of the backscatter component for extracting information about the distance map of the scene. Sec. III describes how we achieve the first goal by polarizing the light source.

[2]Note that $b(\theta)$ and c depend on the wavelength. Thus each available wavelength band is analyzed independently.

[3]As in every asymptotic function, the effective distance can be defined in different ways. For example, it can be defined as the distance where $B_{\text{rel}} = 0.99$.

III. Polarization Imaging

As mentioned earlier, we suggest modulating the light by polarizing the light source and imaging through a camera-mounted polarizer (*analyzer*) in two orthogonal polarization states. The system setup is depicted in Figs. 1 and 5. By mounting a polarizer (either linear or circular) on the light source, we polarize the illumination. The polarized light propagates to illuminate the scene and part of it is scattered back by particles in the medium towards the camera. During this propagation, some energy of the light becomes unpolarized (a process termed *depolarization*). This process is complex and depends on the distribution of particle types and sizes [19], [25], [36]. Apparently, this process affects each polarization type differently: some studies suggest that depolarization during propagation is weaker in circular polarization [19], [25], [29], [36], while Refs. [19], [36] suggest weaker depolarization of linear polarization in dense tissues. An empirical study [44] has looked at the the rate of depolarization with distance in seawater. A preliminary empirical study [11] done decades ago has shown that if the illumination is circularly polarized, then it flips handedness upon backscattering. Thus, Ref. [11] achieved significant improvement in image contrast in an optical method, where it used an analyzer having the same handedness as the illumination polarizer.

That said, despite the scientific efforts that have been invested by various researchers (see for example [33]). The known art has not supplied a clear answer as to which polarization type is preferable in the true environments we worked in, and how the depolarization rate can be determined by the scattering and attenuation coefficients in those environments. Therefore, we tested our method with either linear or circular polarization in different locations. In the case of linear polarization we mount a linear polarizer on the light source and a linear analyzer on the camera. Then, an orthogonal image pair is taken by either rotating the polarizer or the analyzer. Specifically, we chose to rotate the analyzer, as it was easier in our setup. When using circular polarization, orthogonal states result from switching handedness rather than rotating the polarizers. As a consequence, linear polarization is easier to use. Moreover, wideband and widefield circular polarization is difficult to create. In any case, raw polarization data still contains significant backscatter. Therefore, there is a need for post processing, as described in Sec. IV. The post processing we perform does not depend on the polarization type used.

IV. Backscatter Removal by Polarization

This section describes and demonstrates through experiments visibility enhancement by active polarization imaging. This is done by separating the signal and the backscatter components. Later, in Sec. V-A, we explain how the estimated backscatter may be used for estimating the 3D structure of the scene.

A. Model and Algorithm

Former studies have used polarized illumination for backscatter removal. Ref. [50] assumed that objects back-reflect unpolarized light to the camera. On the other hand, studies using polarization difference imaging (PDI) assume the opposite- that the light

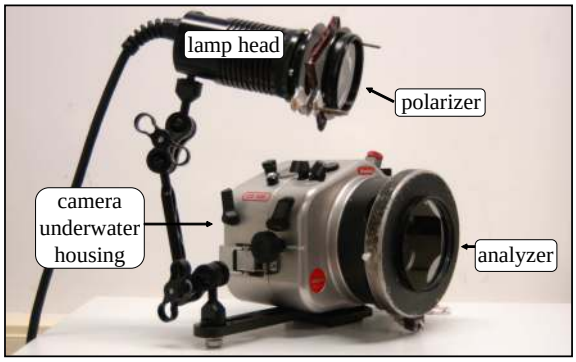

Fig. 5. A single-lamphead version of our system.

reflected from the objects is polarized and that the backscatter is almost unpolarized. Here we give a more general model. Fortunately, if the object yields polarized specular reflection, it behaves similarly to the backscatter: out of the two frames, generally, the one in which the backscatter is brighter is also the one in which the object back-reflection is brighter.[4]

As described in Sec. III, we take two images of the same scene using two orthogonal polarization states of the polarizer. Had the backscattered light completely retained its polarization, it could have been optically eliminated by the analyzer. We discovered that a substantial DOP is maintained upon backscattering. We exploit this phenomenon.[5] Consequently, placing an analyzer in the orthogonal state to the backscatter's polarization state yields an image with minimum visible backscatter. We denote this image as $I^{\min}$. Imaging with the opposite orthogonal state, denoted $I^{\max}$, maximizes the backscatter.

We expand Eq. (2) to the polarized components $B_{\max}, B_{\min}, S_{\max}$ and $S_{\min}$. Thus, the raw images are:

$$\begin{aligned} I_{\max}(\mathbf{x}_{\rm obj}) &= S_{\max}(\mathbf{x}_{\rm obj}) + B_{\max}(\mathbf{x}_{\rm obj}) \quad , \\ I_{\min}(\mathbf{x}_{\rm obj}) &= S_{\min}(\mathbf{x}_{\rm obj}) + B_{\min}(\mathbf{x}_{\rm obj}). \end{aligned} \tag{8}$$

The DOP of the signal $p_{\rm obj}$ and the DOP of the backscatter $p_{\rm scat}$ are defined as:

$$\begin{aligned} p_{\rm obj}(\mathbf{x}_{\rm obj}) &= \frac{S_{\max}(\mathbf{x}_{\rm obj}) - S_{\min}(\mathbf{x}_{\rm obj})}{S_{\max}(\mathbf{x}_{\rm obj}) + S_{\min}(\mathbf{x}_{\rm obj})} \quad , \\ p_{\rm scat}(\mathbf{x}_{\rm obj}) &= \frac{B_{\max}(\mathbf{x}_{\rm obj}) - B_{\min}(\mathbf{x}_{\rm obj})}{B_{\max}(\mathbf{x}_{\rm obj}) + B_{\min}(\mathbf{x}_{\rm obj})}. \end{aligned} \tag{9}$$

In the following $(\mathbf{x}_{\rm obj})$ is omitted for simplicity. We end up with two equations for the two unknown fields - S and B:

$$\mathbf{I}_{\max} + \mathbf{I}_{\min} = \mathbf{B} + \mathbf{S} \tag{10}$$

$$\mathbf{I}_{\max} - \mathbf{I}_{\min} = p_{\rm scat}\mathbf{B} + p_{\rm obj}\mathbf{S}. \tag{11}$$

The last equation is derived from plugging Eq. (9) into Eq. (8). The solution to this equation set is:

$$\hat{\mathbf{S}} = \frac{1}{p_{\rm scat} - p_{\rm obj}}[\mathbf{I}_{\min}(1 + p_{\rm scat}) - \mathbf{I}_{\max}(1 - p_{\rm scat})] \tag{12}$$

$$\hat{\mathbf{B}} = \frac{1}{p_{\rm scat} - p_{\rm obj}}[\mathbf{I}_{\max}(1 - p_{\rm obj}) - \mathbf{I}_{\min}(1 + p_{\rm obj})]. \tag{13}$$

[4]Empirically, we never encountered a reversed polarization of the signal relative to the backscatter.

[5]Polarization has also aided other computer vision aspects [2], [5], [7], [8], [27], [40], [43], [45], [54].

This is a general result, enabling separation of $\mathbf{B}$ and $\mathbf{S}$ from the two raw images, given the DOPs $p_{\rm obj}$ and $p_{\rm scat}$.

A very important property of Eq. (12) is that $p_{\rm obj}$ contributes only a scale factor to the signal reconstruction $\hat{\mathbf{S}}$. Suppose that $p_{\rm obj}$ is approximately constant across the scene, but it is unknown. Then, the signal estimation (12) is consistent with the true $\mathbf{S}$ up to a scale. For purposes of visibility enhancement, the scaled $\hat{\mathbf{S}}$ is sufficient: the backscatter is removed, and missing parts are revealed. Furthermore, the backscatter is usually not uniform across the image; some regions have high intensity backscatter, and others have low intensity backscatter (see Fig. 2). This hampers standard image enhancement techniques. Therefore, removing the backscatter results in a signal estimation $\hat{\mathbf{S}}$ with a more uniform intensity. Thus, further image improvement may be obtained by applying standard image enhancement techniques to $\hat{\mathbf{S}}$, rather than applying them to $\mathbf{I}$ or $\mathbf{I}_{\min}$.

As $p_{\rm obj}$ changes only the scale of $\hat{\mathbf{S}}$, good results can be achieved [38], [39], [41], [50] based on the assumption that $p_{\rm obj} = 0$. In this case, Eqs. (12,13) reduce to:

$$\hat{\mathbf{S}} = [\mathbf{I}_{\min}(1 + p_{\rm scat}) - \mathbf{I}_{\max}(1 - p_{\rm scat})]/p_{\rm scat} \tag{14}$$

$$\hat{\mathbf{B}} = (\mathbf{I}_{\max} - \mathbf{I}_{\min})/p_{\rm scat}. \tag{15}$$

Note, that in this case,

$$\mathbf{I}_{\min} = [\mathbf{B}(1 - p_{\rm scat}) + \mathbf{S}]/2 \ , \ \mathbf{I}_{\max} = [\mathbf{B}(1 + p_{\rm scat}) + \mathbf{S}]/2. \tag{16}$$

Let us examine the consequence of using an assumption $p_{\rm obj} = 0$ in Eq. (13), when image creation (Eq. 8) experienced $p_{\rm obj} \neq 0$. This case yields a false estimation $\tilde{\mathbf{B}}$ of the backscatter,

$$\tilde{\mathbf{B}} = \frac{\mathbf{I}_{\max} - \mathbf{I}_{\min}}{p_{\rm scat}} = \hat{\mathbf{B}} + \frac{\mathbf{S}_{\max} - \mathbf{S}_{\min}}{p_{\rm scat}} = \hat{\mathbf{B}} + \frac{p_{\rm obj}}{p_{\rm scat}}\mathbf{S}. \tag{17}$$

The last equality results from plugging in the DOP $p_{\rm obj}$ from Eq. (9). As discussed in Sec. II, $\mathbf{B}$ increases with the distance. From Eq. (5), when the camera and the light sources are on the same side of the object (a common scenario), S decreases with the distance. In that case, a result of Eq. (17) is that $\tilde{\mathbf{B}}$ is no longer monotonic with $Z_{\rm obj}$.

As opposed to the assumption $p_{\rm obj} = 0$, methods based on PDI [52] assume that $p_{\rm scat}/p_{\rm obj} \to 0$. Plugging $p_{\rm scat}/p_{\rm obj} \to 0$ to Eqs. (12,13) results in:

$$\hat{\mathbf{S}} = \frac{1}{p_{\rm obj}}[\mathbf{I}_{\max} - \mathbf{I}_{\min}] \quad , \tag{18}$$

$$\hat{\mathbf{B}} = \frac{1}{p_{\rm obj}}[\mathbf{I}_{\min}(1 + p_{\rm obj}) - \mathbf{I}_{\max}(1 - p_{\rm obj})]. \tag{19}$$

Note that in this case, Eq. (18) is a scaled version of the polarization difference image. Here we see that Eqs. (12,13) unify both the dehazing methods [38], [39], [41], [50], where $p_{\rm obj} = 0$, and the PDI methods where $p_{\rm scat}/p_{\rm obj} \to 0$.

Using Eqs. (12,13) without such approximations requires the estimation of the DOPs. Sec. VI describes how the DOPs are estimated in the general case. First, however, we demonstrate backscatter removal in experiments.

B. Experiments

The method described above is general and it does not assume a specific medium. However, as discussed in Sec. III, depolarization depends on the medium [22]. Therefore, in order to demonstrate the effectiveness of the method in real world

Fig. 6. [Left] Scuba diving with a lift-bag, towards night experiments in the Red Sea. [Right] Preparations for an experiment in the Mediterranean.

situations, we embarked on underwater dives rather than using indoor tanks. Particles in substances (like milk, lipids, etc.) used for diluting water in indoor tanks are usually homogeneous and sometimes symmetric [19], [35] while oceanic particles are heterogeneous [28]. Therefore, we were concerned that polarization experiments done with diluted substances would not represent correctly the properties and the variety of the media in the field, e.g., seawater. We have done experiments while scuba diving at night in various environments, in a pool, the Red Sea, the Mediterranean (Fig. 6) and the Sea of Galilee.

C. Equipment

Fig. 5 shows the system we used has two main parts:

- An SLR camera with an underwater housing. We use a Nikon D100 camera, which has a linear response [38], [39]. The camera is placed in a Sealux underwater housing with a mounted polarizer. The considerations for choosing a camera, an underwater housing and mounted polarizers are detailed in [38], [39].
- Underwater AquaVideo light sources, with 80W Halogen bulbs. A polarizer is mounted on the lighthead. We had special consideration behind the selection of the lighting setup, as detailed in the appendix.

We used standard off-the-shelf polarizers of Schneider and Tiffen. The camera was mounted on a tripod. To safely transport this amount of equipment while diving, a 50kg lift-bag was used (Fig. 6). The tripod was set to resist swell by attaching weights on its lower part.

D. Real World Results

Fig. 7 shows the results of applying Eqs. (14,15) on images taken during four different experiments we have performed. We tested the method using different light source locations. The left column presents the raw images $\mathbf{I}$. The center column shows $\hat{\mathbf{S}}$ (where the estimated backscatter is removed). The right column shows the estimated backscatter component $\hat{\mathbf{B}}$. The experiments in the three top rows were performed in the Mediterranean on three different occasions. In all three cases, using linear polarizers have yielded a DOP of $p_{\rm scat} \approx 65\%$. In **experiment 1** we used two light sources, shining from above and below the camera. Here, $Z_{\rm obj} < 3m$. Notice the revealed rock in the upper left part, the sand in the right side, the rocks on the bottom and the distant part of the tube. In **experiment 2**, $Z_{\rm obj} \in [0.5m, 6m]$. Here, we used a single light source, coming from the top right. Notice the revealed rectangular cube in the background. The revealed objects in the background are dark, as at this distance they receive only dim irradiance from the sources. **Experiment 3** shows a scene illuminated from the bottom right. Consequently, the lower parts have a lot of backscatter, hence poor visibility. Our method enhanced the visibility in this part.

Experiment 4 shows a result of an experiment done in the Sea of Galilee, a very murky lake. The light source is placed above the camera. Here, $Z_{\rm obj} \approx 0.5m$, which was the maximum visibility distance. Here, circular polarization yielded $p_{\rm scat} \approx 9\%$ while linear polarization yielded $p_{\rm scat} \approx 5\%$. Despite the difficult conditions, the method revealed the imaged object, its rough contour and its colors. Notice that in both **experiments 2** and **4**, the upper part of the raw frame is very bright, due to backscatter. This may cause the viewer to falsely assume there is a bright object in that part of the scene. After removal of the backscatter, these areas become dark, as there is actually no light reflecting from objects there. Then, we expect the scene radiance to act according to Eq. (5). Indeed, in **experiment 2**, the brightest part of $\hat{\mathbf{S}}$ is the lower, close sand.

In our field experiments, both polarization types (linear and circular) yielded good results. When visibility was moderate (in the Mediterranean), linear polarization retained $p_{\rm scat} \approx 60-70\%$, higher than circular polarization, for which $p_{\rm scat} \approx 50\%$. In the murky Sea of Galilee, on the other hand, circular DOP was higher than the linear one. There, perceptual difference hardly existed between the raw frames, due to the low DOP value. Nevertheless, our method still enhanced $\hat{\mathbf{S}}$ significantly.

V. Range and Falloff

A. Range

Let us have an estimate for the backscatter $\hat{\mathbf{B}}$ in a scene, for example, using the method in Sec. IV. We would like to know if we may leverage $\hat{\mathbf{B}}$ to estimate the 3D structure of the scene. A general approach is presented for estimating $Z_{\rm obj}$ based on $\hat{\mathbf{B}}$. It does not depend on the algorithm used for extracting $\hat{\mathbf{B}}$ itself.

Similarly to [4], [30], [38], [39], [41], the backscatter B increases with the distance $Z_{\rm obj}$, hence it can indicate the distance. Previously [38], [39], [41], this principle was developed in the

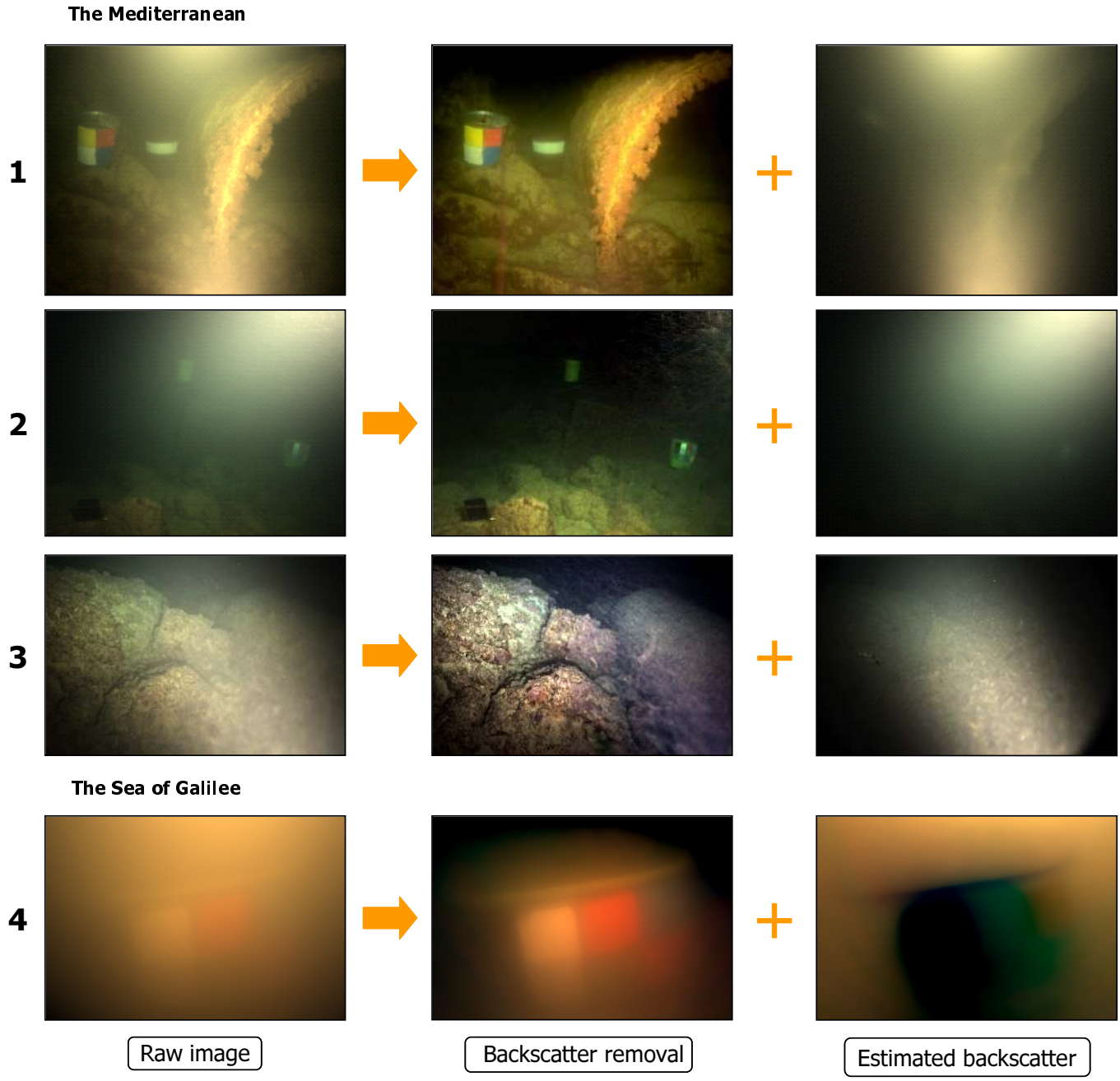

Fig. 7. Results of four different experiments. [Left] The raw images $\mathbf{I}$. [Middle] The recovered signals $\hat{\mathbf{S}}$. [Right] The estimated backscatter fields $\hat{\mathbf{B}}$.

simple special case of distant illumination sources (natural light), where the following relation holds:

$$B = B_\infty\{1 - \exp[-cR_{\rm cam}(x, y, Z_{\rm obj})]\} \approx B_\infty\{1 - \exp[-cZ_{\rm obj}(x, y)]\}. \quad (20)$$

Such an estimation can be generalized to the use of sources close to the camera. We found numerically [50] that in widefield lighting, Eq. (7) can be approximated as

$$B(\mathbf{x}_{\rm obj}) \approx B_\infty(\mathbf{x}_{\rm obj}) \cdot \left(1 - \exp[-\left\{-k(\mathbf{x}_{\rm obj})[Z_{\rm obj}(\mathbf{x}_{\rm obj}) - Z_0(\mathbf{x}_{\rm obj})]\right\}]\right), \quad (21)$$

resembling Eq. (20). Fig. 8 presents an approximation done for a particular setup. A major difference between Eqs. (20) and (21) is that in Eq. (21) B_∞ is space variant. Eq. (21) introduces two new space-variant parameters, $Z_0(\mathbf{x}_{\rm obj})$ and $k(\mathbf{x}_{\rm obj})$. The offset Z_0 is a distance, which indicates the first effective intersection of the LOS with the light cone emitted by the lamphead. The rate in which B increases with $Z_{\rm obj}$ at Z_0 is set by k. These parameters (B_∞, Z_0, k) depend on the lighting geometry, the non-uniformity (anisotropy) $Q(\mathbf{X}_{\rm obj})$ of the illumination sources and on the medium parameters c and b (described in Sec. II). They do *not* depend on $Z_{\rm obj}$.

Eq. (21) is easy to invert, deriving an estimate $\hat{Z}_{\rm obj}(\mathbf{x}_{\rm obj})$ as

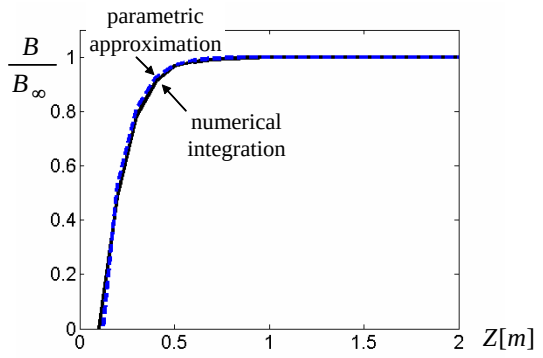

Fig. 8. The backscatter given by Eq. (7) as approximated by Eq. (21), with $c = 0.1m^{-1}$.

a function of $\hat{B}(\mathbf{x}_{\rm obj})$:

$$\hat{Z}_{\rm obj}(\mathbf{x}_{\rm obj}) = Z_0(\mathbf{x}_{\rm obj}) - \left[\ln\left(1 - \frac{\hat{B}(\mathbf{x}_{\rm obj})}{B_\infty(\mathbf{x}_{\rm obj})}\right)\right]\frac{1}{k(\mathbf{x}_{\rm obj})}. \quad (22)$$

This, of course, requires calibration of the spatially varying parameter fields $\mathbf{B}_\infty$, $\mathbf{k}$ and $\mathbf{Z}_0$. An important parameter is B_∞. It expresses the backscatter at $\mathbf{x}_{\rm obj}$, had there been no object in the LOS. Therefore, the relation

$$B_{\rm rel}(\mathbf{x}_{\rm obj}) = \frac{\hat{B}(\mathbf{x}_{\rm obj})}{B_\infty(\mathbf{x}_{\rm obj})}, \quad (23)$$

indicates how much the backscatter has reached its saturation value B_∞. Thus, $B_{\rm rel}$ is monotonic with $Z_{\rm obj}$. The parameters k and Z_0 function as scaling factors in Eq. (22). It is easy [50] to determine the field $\mathbf{B}_\infty$ by taking a photograph in the medium, where the camera is pointing "no-where" (to infinity). By approximating $\mathbf{k}$ and $\mathbf{Z}_0$ to be uniform and plugging in typical values for them in Eq. (22), a rough distance map can be estimated.

We simulated similar setups to those we used in our experiments. To simplify the analysis, let us assume that the backscatter coefficient $b(\theta)$ is uniform in the range of angles we use. This assumption is supported by [22], which shows that in oceanic water the function $b(\theta)$ is insensitive to θ at backscatter angles ($\theta \geq \pi/2$). Fig. 9 shows a distance map derived by applying Eqs. (22,23) on an underwater scene. For Eq. (22) we used the values $Z_0 = 20cm$ and $k = 0.6$. Those values were chosen based on a numerical analysis of setups where the light source was in proximity to the camera. This analysis showed that Z_0 ranges between $10cm - 30cm$ and k ranges between $3 - 6$. The value of k changes between different illumination-camera setups. It also changes spatially in the image, pixels closer to the light source having a higher k.

B. Falloff

Sec. V-A described the estimation of $\hat{Z}_{\rm obj}(\mathbf{x}_{\rm obj})$. Based on $\hat{Z}_{\rm obj}(\mathbf{x}_{\rm obj})$, we may now estimate the falloff, using Eq. (5). Here we need three additional parameters. First is the attenuation coefficient c, which can be measured by a transmissiometer. Second, we need $Q(\mathbf{X}_{\rm obj})$. This can be pre-calibrated once per light source. In addition, there is a need to know $R_{\rm source}$. It is derived based on *a-priori* knowledge about the system baseline [48]: it is sufficient to know the camera-light-source baseline $R_{\rm sc}$, and the angle between this source and the LOS, γ (See Fig. 1). Then,

$$R_{\rm source} = \sqrt{R_{\rm sc}^2 + R_{\rm cam}^2 - 2R_{\rm cam}R_{\rm sc}\cos\gamma}. \quad (24)$$

The value of $\hat{R}_{\rm cam}$ is estimated by setting $z = \hat{Z}_{\rm obj}$ in Eq. (4). Then Eq. (24) derives $\hat{R}_{\rm source}$. The use of $\hat{Z}_{\rm obj}$ and $\hat{R}_{\rm source}$ in Eq. (5), derives an estimate for the falloff $\hat{F}(\mathbf{x}_{\rm obj})$. Compensating for the falloff by inverting Eq. (3) yields

$$\hat{L}_{\rm object}(\mathbf{x}_{\rm obj}) = \hat{S}(\mathbf{x}_{\rm obj})/\hat{F}(\mathbf{x}_{\rm obj}). \quad (25)$$

To illustrate this, Fig. 10 shows a simulation of the entire recovery method. A simulated object was assigned a non-trivial distance map and artificial noise was added with standard deviation of $\sigma_{I_{\rm min}} = \sigma_{I_{\rm max}} = 1$ grey level (out of 256 gray levels in the raw frames $\mathbf{I}_{\rm min}$, $\mathbf{I}_{\rm max}$). Fig. 10d shows $\hat{L}_{\rm object}(\mathbf{x}_{\rm obj})$ after both removal of the estimated backscatter and falloff compensation. While the image is enhanced relative to the simulated I, there is noise amplification in the distant parts [20], [37].

VI. Estimation of the DOPs

In Sec. IV we use the parameters $p_{\rm scat}$ and $p_{\rm obj}$ to reconstruct $\mathbf{S}$ and $\mathbf{B}$. Ways for estimating these parameters are discussed now.

A. Extraction of $p_{\rm scat}$

Light depolarizes as it propagates [44]. Therefore, it is reasonable to expect the measured $p_{\rm scat}$ to be nonuniform. The reason for this is that backscattered light from a large $Z_{\rm obj}$ contributes $p_{\rm scat}$ that is smaller than light backscattered from a small $Z_{\rm obj}$. In total, the measured $p_{\rm scat}$ is influenced by light that is backscattered from all distances (up to the object), close and far, on the LOS. However, we found empirically that the value of $p_{\rm scat}$ is practically constant across the field of view (FOV) in seawater.[6] A possible explanation to this phenomenon is demonstrated in Figs. (8,16): after a short distance, the backscatter is saturated. Therefore, backscatter stemming from large distances (with a low $p_{\rm scat}$) has almost no influence on the measurement.

As $p_{\rm scat}$ is practically uniform, it is easy to measure. It can be retrieved in several distinct ways. These include:

1) Measuring an area $\mathbf{x}_{\rm void}$ in the FOV in which there is no signal. Since there is no object in $\mathbf{x}_{\rm void}$, then $\mathbf{I}_{\rm max}(\mathbf{x}_{\rm void}) = \mathbf{B}_{\rm max}(\mathbf{x}_{\rm void})$ and $\mathbf{I}_{\rm min}(\mathbf{x}_{\rm void}) = \mathbf{B}_{\rm min}(\mathbf{x}_{\rm void})$. Thus,
$$\hat{p}_{\rm scat}(\mathbf{x}_{\rm void}) = \frac{I_{\rm max}(\mathbf{x}_{\rm void}) - I_{\rm min}(\mathbf{x}_{\rm void})}{I_{\rm max}(\mathbf{x}_{\rm void}) + I_{\rm min}(\mathbf{x}_{\rm void})}. \quad (26)$$
Assuming that $p_{\rm scat}$ is uniform across the scene, Eq. (26) yields an estimation of $p_{\rm scat}$ for the entire FOV.
2) Rigidly shifting the camera/illuminator system, to point to a void region in the medium (where no object is in sight), as in Sec. V-A. Then, an image pair $\mathbf{I}_{\rm max}, \mathbf{I}_{\rm min}$ is acquired. In this case, every pixel points to a void. Therefore, using this pair with Eq. (26) yields a potentially spatially varying $p_{\rm scat}$. This method enables a more flexible model.

Let us analyze the consequences of a mistake in the estimation of $p_{\rm scat}$, i.e.

$$\hat{p}_{\rm scat} = \psi p_{\rm scat}^{\rm true}, \quad (27)$$

where $p_{\rm scat}^{\rm true}$ is the true backscatter DOP. Underestimation and overestimation correspond to $\psi < 1$ and $\psi > 1$, respectively. If

[6] We found it is constant up to $\approx 24^\circ$ relative to the optical axis.

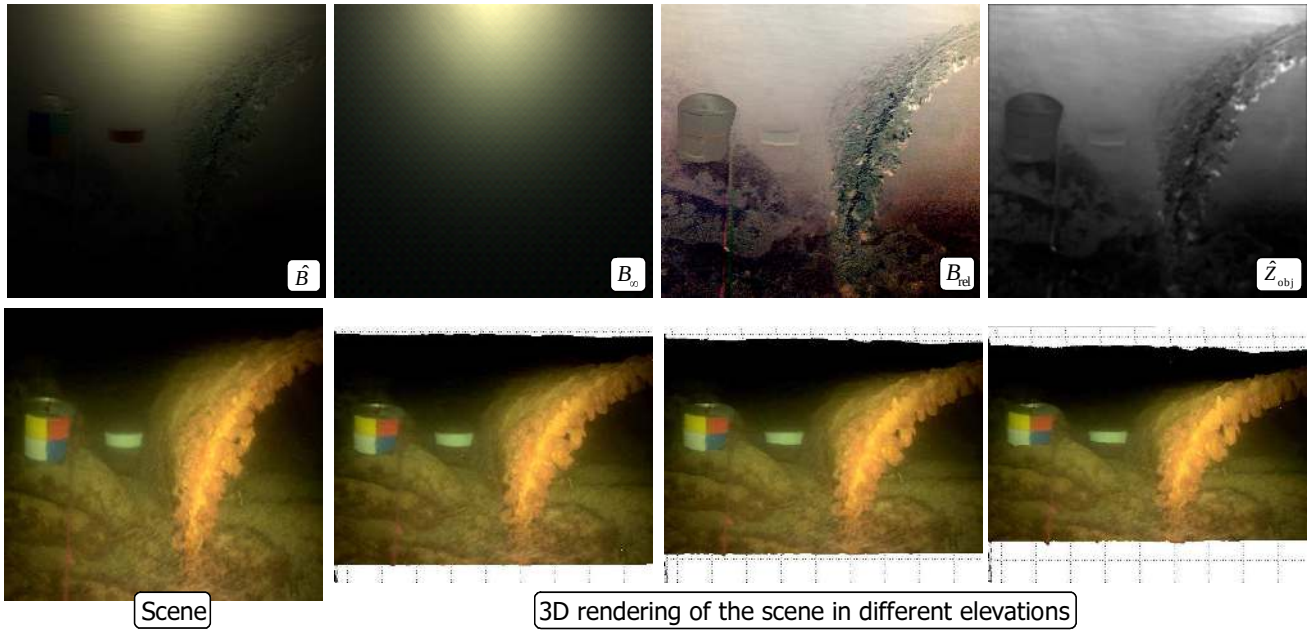

Fig. 9. Estimation of a distance map. [Top] The different components of Eqs. (21,23) in an underwater experiment. The image $\mathbf{B}_{\text{rel}}$ is scaled to yield an estimation of the distance map. [Bottom] Views from different elevations of the reconstructed 3D scene composed of the recovered signal and the estimated distance map.

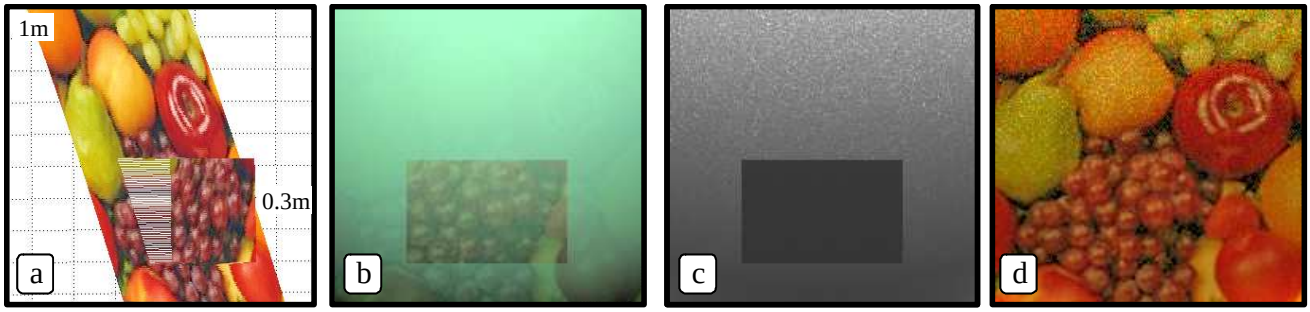

Fig. 10. Simulated backscatter removal, 3D recovery and falloff compensation of a noisy object. (a) An object was assigned a distance map varying linearly to $1m$ with a sticking rectangle at a distance of $0.3m$. (b) The simulated underwater raw frame $\mathbf{I}$, with added noise. (c) The estimated distance map $\hat{\mathbf{Z}}_{\text{obj}}$. (d) The recovered object radiance $\hat{\mathbf{L}}_{\text{obj}}$. In (c) and (d) the noise is amplified in the distant parts.

$p_{\text{obj}} = 0$, then using Eq. (27) in Eq. (15) yields an erroneous estimate

$$\tilde{\mathbf{B}} = \frac{\mathbf{I}_{\max} - \mathbf{I}_{\min}}{\psi p_{\text{scat}}^{\text{true}}} = \frac{1}{\psi}\mathbf{B}. \tag{28}$$

Similarly, the signal is erroneously estimated as

$$\tilde{\mathbf{S}} = \mathbf{I} - \frac{1}{\psi}\mathbf{B} = \mathbf{S} + \left(1 - \frac{1}{\psi}\right)\mathbf{B}. \tag{29}$$

The relative backscatter error

$$\mathbf{E}_B^{\text{rel}} = \left|\frac{\tilde{\mathbf{B}} - \mathbf{B}}{\mathbf{B}}\right| = |1/\psi - 1| \tag{30}$$

is constant over the FOV. On the other hand,

$$\mathbf{E}_S^{\text{rel}} = \left|\frac{\tilde{\mathbf{S}} - \mathbf{S}}{\mathbf{S}}\right| = |1/\psi - 1|\,\frac{B(\mathbf{x}_{\text{obj}})}{S(\mathbf{x}_{\text{obj}})} \tag{31}$$

depends on $B(\mathbf{x}_{\text{obj}})/S(\mathbf{x}_{\text{obj}})$. Generally B/S increases with Z_{obj}, hence $\tilde{S}$ is more affected by this error. Fig. 11 depicts $|1/\psi - 1|$, which is the part that depends on ψ in $\mathbf{E}_B^{\text{rel}}$ and

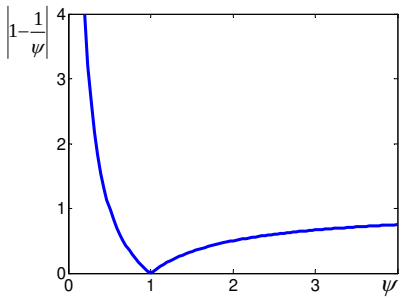

Fig. 11. Influence of a wrongly estimated p_{scat}. The relative error is typically smaller in overestimation of p_{scat} than in underestimation.

$\mathbf{E}_S^{\text{rel}}$. From Fig. 11, the relative error is typically smaller when $\psi > 1$. Therefore, it is better to overestimate p_{scat} rather than underestimating it.

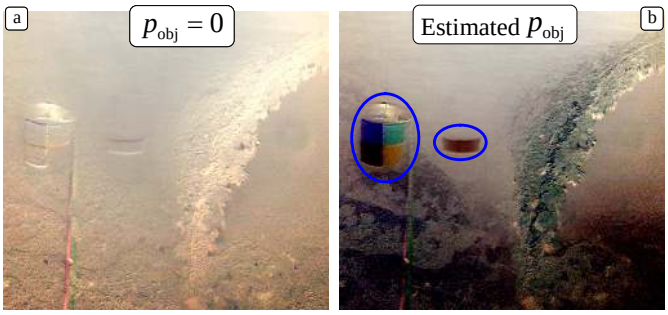

Fig. 12. An image of $\hat{\mathbf{B}}_{\text{rel}}$ in an underwater scene. (a) When assuming $p_{\text{obj}} = 0$, areas in proximity to the camera (lower part of the image) are falsely assigned a high value. (b) Using an estimated p_{obj} reveals that $\hat{\mathbf{B}}_{\text{rel}}$ is indeed low at close distances. Here p_{obj} is assumed to be spatially uniform. Areas that do not comply with this assumption stand out (blue ellipses).

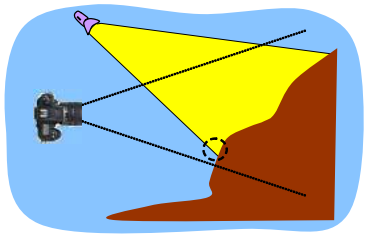

Fig. 13. Off axis illumination results in areas with low backscatter (the circled part). This area can be sampled to estimate $\hat{p}_{\text{obj}}$.

B. Estimating p_{obj}

Sec. IV shows that for purposes of signal reconstruction, it is possible to assume that $p_{\text{obj}} = 0$. However, from Eq. (13), if this assumption is wrong, it damages the estimation of $\hat{\mathbf{B}}$. As a consequence, it damages the estimation of the object distances $\mathbf{Z}_{\text{obj}}$, based on $\hat{\mathbf{B}}$, as described in Sec. V-A. Failing to estimate p_{obj} correctly, damages the monotonic relation between $\hat{\mathbf{B}}$ to Z_{obj} expressed in Eq. (21). For illustration, in a real scene which we present in the following, $p_{\text{obj}} \approx 30\%$ at the rocks. In Fig. 12(a) $\hat{\mathbf{B}}_{\text{rel}}$ is estimated under the wrong assumption that $\hat{p}_{\text{obj}} = 0$. Here, $\hat{\mathbf{B}}_{\text{rel}}$ is rather uniform, despite variations of Z_{obj}. On the other hand, when taking into consideration $p_{\text{obj}} \approx 30\%$, Fig. 12(b) reveals the significant dependency of $\hat{B}_{\text{rel}}$ on Z_{obj} in this case.

Sometimes p_{obj} can be sampled directly from the images. Consider the marked circle in Fig. 13, in off-axis illumination, the objects at the far fringe of the irradiated spot are lit, but are effectively not veiled by backscatter (as in [31]).

In Fig. 14(a), for example, this occurs in the upper left part of the FOV. Term such an image location as $\mathbf{x}_{\text{clear}}$. In such areas, $\mathbf{I}_{\max} \approx \mathbf{S}_{\max}$ and $\mathbf{I}_{\min} \approx \mathbf{S}_{\min}$. Then, similarly to Eq. (26),

$$\hat{p}_{\text{obj}} = \frac{I_{\max}(\mathbf{x}_{\text{clear}}) - I_{\min}(\mathbf{x}_{\text{clear}})}{I_{\max}(\mathbf{x}_{\text{clear}}) + I_{\min}(\mathbf{x}_{\text{clear}})}. \tag{32}$$

For example, in the scene presented in Fig. 14, the measured values of $\hat{p}_{\text{obj}}$ in the red, green and blue channels are $0.22, 0.27$ and 0.34 respectively.

1) Automatic Estimation: We discuss here an automatic approach for the estimation of p_{obj}. It is based on the observation that using a wrong value for p_{obj} increases the crosstalk between the estimated backscatter $\hat{\mathbf{B}}$ and the signal component $\hat{\mathbf{S}}$. Let

$$\hat{p}_{\text{obj}} = p_{\text{obj}}^{\text{true}} + \varepsilon, \tag{33}$$

where ε is the error in p_{obj}. Using Eq. (33) in Eq. (12,13) , yields an erroneous estimate of $\mathbf{B}$,

$$\tilde{\mathbf{B}} = \mathbf{B} - \frac{\varepsilon}{p_{\text{scat}} - p_{\text{obj}}^{\text{true}}}\tilde{\mathbf{S}}, \tag{34}$$

where $\tilde{\mathbf{S}}$ is the erroneous estimate of $\mathbf{S}$. Note that Eq. (17) is a special case of Eq. (34), in which $p_{\text{obj}}^{\text{true}} = p_{\text{obj}}$ and $\varepsilon = -p_{\text{obj}}$. In any case, Eq. (34) shows that there is crosstalk between $\tilde{\mathbf{B}}$ and $\tilde{\mathbf{S}}$ that increases with ε. For example, Fig. 14(b) shows $\hat{\mathbf{B}}$ calculated using the assumption that $p_{\text{obj}} = 0$ (Eq. 15). Note that the value of $\hat{\mathbf{B}}$ in the circled area is high. In fact, a rock from $\mathbf{I}$ can be seen there. Fig. 14(c) shows $\mathbf{B}_\infty$ for this setup. The value of the circled part in $\hat{\mathbf{B}}$ is almost as high as its value in $\mathbf{B}_\infty$. This falsely indicates a far object.

To quantify the crosstalk, we may use mutual information (MI). The MI is a quantity that measures mutual statistical dependency of the two random variables $\tilde{B}$ and $\tilde{S}$. A high value indicates some statistical dependency between the variables. Define b as a gray level in the image $\tilde{\mathbf{B}}$. Similarly, define s as a gray level in the image $\tilde{\mathbf{S}}$. Then,

$$\text{MI}(\tilde{\mathbf{B}}, \tilde{\mathbf{S}}) = \sum_{b \in \tilde{\mathbf{B}}} \sum_{s \in \tilde{\mathbf{S}}} \texttt{prob}(b,s) \log \left[\frac{\texttt{prob}(b,s)}{\texttt{prob}(b)\texttt{prob}(s)} \right], \tag{35}$$

where $\texttt{prob}(b,s)$ is the joint probability distribution function of pixels in $\tilde{\mathbf{B}}$ and $\tilde{\mathbf{S}}$. The marginal distribution functions of $\tilde{\mathbf{B}}$ and $\tilde{\mathbf{S}}$ are defined as $\texttt{prob}(b)$ and $\texttt{prob}(s)$, respectively. The true distribution functions are unknown and therefore they are estimated using histograms, or, more efficiently, by Parzen windows [46]. Thus, we estimate an optimal value for $\hat{p}_{\text{obj}}$ as

$$\hat{p}_{\text{obj}}^{\text{optimal}} = \arg \min_{\hat{p}_{\text{obj}} \in [0,1]} \left\{ \text{MI}\left[\tilde{\mathbf{B}}(\hat{p}_{\text{obj}}), \tilde{\mathbf{S}}(\hat{p}_{\text{obj}}) \right] \right\}. \tag{36}$$

In the experiment shown in Fig. 14, the MI for different potential values of $\hat{p}_{\text{obj}}$ is plotted in Figs. 14(e,f). In each color channel, there is one value of $\hat{p}_{\text{obj}}$ that minimizes the MI. Note that these values are *very close* to the values acquired by sampling (Eq. 32). These values were used in Eq. (13) to calculate $\hat{\mathbf{B}}$ in Fig. 14(d). It shows $\hat{\mathbf{B}}$ based on Eq. (13), using the value $p_{\text{obj}}^{\text{optimal}}$ derived by Eq. (36). Now the circled part has a low value of $\hat{B}$, as expected from a close object. Another example for the automatic estimation is shown in Fig. 15.

The problem becomes more complicated when p_{obj} varies across the scene. In Fig. 12 we can see (in blue ellipses) two objects whose p_{obj} is significantly different than the rest of the objects. It causes distortions in the backscatter image. In this case, we assigned for these objects the value of $\hat{B}_{\text{rel}}$ of their surrounding, in order to get an estimation of the distance map which is shown in Fig. 9.

VII. Effectiveness Under Noise

Secs. IV-VI described methods to recover the object visibility and distance. An important question to ask is how distant can objects be, and still be recovered? Even in a non-scattering medium, widefield illumination is limited by the free-space falloff term $1/R_{\text{source}}^2$. This poses an inherent limit on all approaches that use widefield illumination. Objects at long distances, which

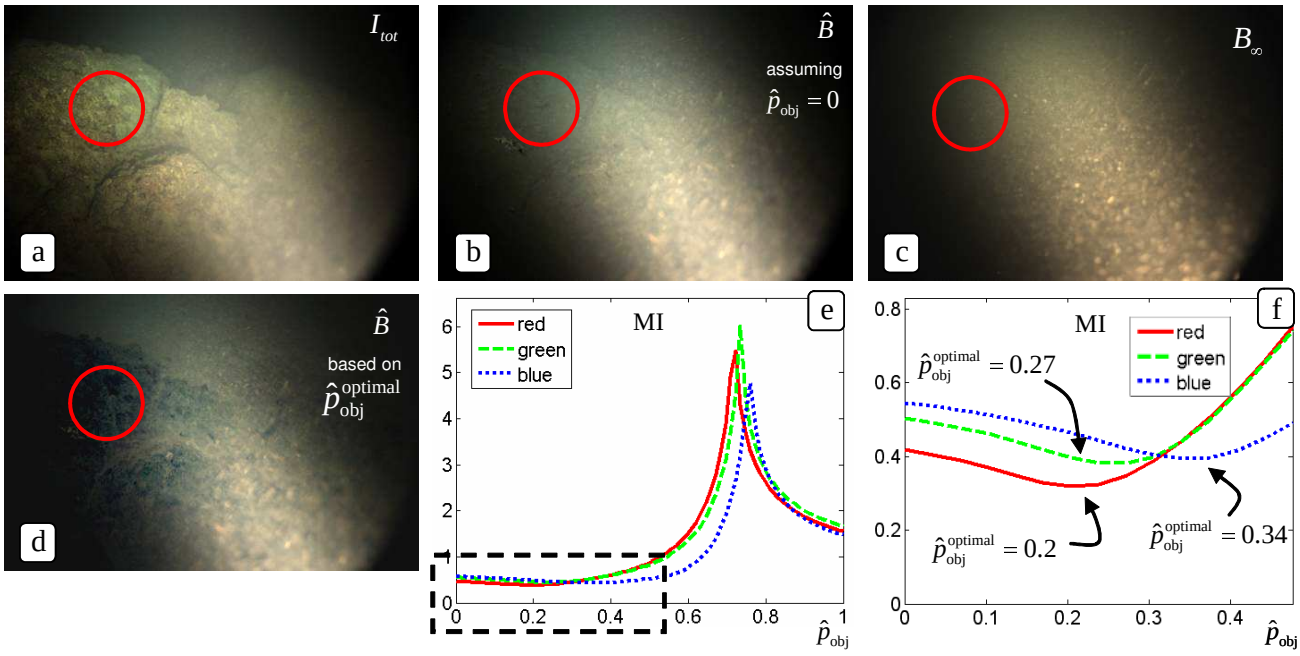

Fig. 14. (a) A raw image $\mathbf{I}$ of an underwater scene. (b) The estimated $\hat{\mathbf{B}}$ using the assumption that $\hat{p}_{\rm obj} = 0$. (c) $\mathbf{B}_\infty$ of that setup. (d) $\hat{B}$ using an estimation for $\hat{p}_{\rm obj}$. (e) The MI of $\hat{\mathbf{B}}$ and $\hat{\mathbf{S}}$ as a function of $\hat{p}_{\rm obj}$. In each color channel, the minimum of the MI sets $\hat{p}_{\rm obj}^{\rm optimal}$. (f) Zoom into the marked part of plot (e).

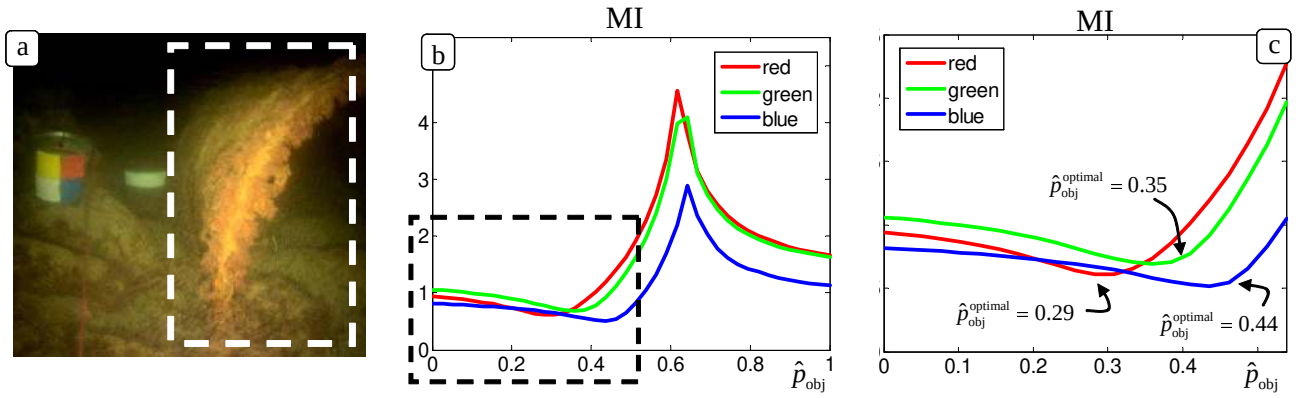

Fig. 15. Using Eq. (36) on the example of Fig. 9. The MI was calculated only on the part marked by the white rectangle in (a), to avoid the anomalous objects on the left part of (a). The full plot is shown in (b). Zoom-in of the marked rectangle in (b) is shown in (c).

are not lit effectively, cannot be reconstructed. Moreover, no imaging system is free of noise. As a consequence, when the signal is in the order of the noise, reconstruction is limited. For example, in our system, the recorded intensity of objects farther than $6 - 7[m]$ was too low to be recovered by removing the backscatter component.

As for distance recovery, a major concern is the resolution of the function $\hat{B}(Z_{\rm obj})$. The function in Eq. (21) is approximately linear at short distances, yielding a good distance resolution. However, Eq. (21) saturates very quickly, thus losing the capacity of proper recovery. Again, when the resolution is in the magnitude of the noise, the reconstruction may become fruitless. What are the typical saturation distances? Fig. 16 depicts $\mathbf{B}_{\rm rel}$ as a function of the object distance. It is a result of simulations based on three classes of values for b and c, taken from [28], which are typical to seawater at different environments. The simulated light source was placed $15cm$ from the optical axis of the camera. Recall (Sec. II) that the saturation distance $z_{\rm sat}$ is the distance in which B effectively becomes indistinguishable from B_∞. We can see that $z_{\rm sat}$ does not vary much with the water properties. In either case, beyond $\approx 1.5[m]$ the backscatter is already saturated and is thus uninformative with respect to $Z_{\rm obj}$. Therefore, accurate distance reconstruction based on backscatter is limited to the close distances. Moreover, in all the simulated water types, $Z_{\rm sat} \ll c^{-1}$. Sections VII-A and VII-B analyze the limits as a function of various medium and imaging parameters.

A. $\hat{S}$ and $\hat{B}$

Suppose we have two statistically independent intensity measurements, $I_{\max}$ and $I_{\min}$ with noise variances $\sigma^2_{I_{\max}}$ and $\sigma^2_{I_{\min}}$ respectively. Let variable v be a function of $I_{\max}$ and $I_{\min}$. Then,

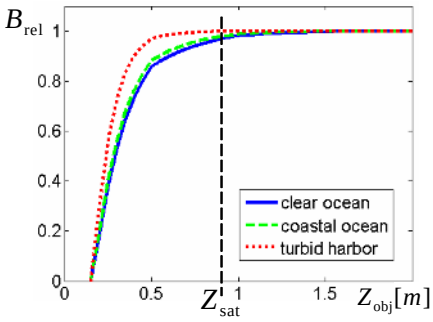

Fig. 16. The relative backscatter $\mathbf{B}_{\text{rel}}$ as a function of the object distance. The values for b and c are taken from [28]. The backscatter saturates within a range of $1.5m$. Moreover, the saturation distance Z_{sat} is similar in all three different water types.

in a first order approximation, the noise variance of v is given by

$$\sigma_v^2 = \left(\frac{\partial v}{\partial I_{\min}}\right)^2 \sigma_{I_{\min}}^2 + \left(\frac{\partial v}{\partial I_{\max}}\right)^2 \sigma_{I_{\max}}^2. \tag{37}$$

According to Eqs. (12,13), the variables $\hat{S}$ and $\hat{B}$ linearly depend on $I_{\min}$ and $I_{\max}$. Therefore, with respect to these variables, Eq. (37) is an exact expression. Following Eqs. (12,13), the noise variances in $\hat{\mathbf{S}}$ and $\hat{\mathbf{B}}$ are:

$$\sigma_{\hat{S}}^2 = \left(\frac{1+p_{\text{scat}}}{p_{\text{obj}}-p_{\text{scat}}}\right)^2 \sigma_{I_{\min}}^2 + \left(\frac{1-p_{\text{scat}}}{p_{\text{obj}}-p_{\text{scat}}}\right)^2 \sigma_{I_{\max}}^2 \tag{38}$$

$$\sigma_{\hat{B}}^2 = \left(\frac{1+p_{\text{obj}}}{p_{\text{obj}}-p_{\text{scat}}}\right)^2 \sigma_{I_{\min}}^2 + \left(\frac{1-p_{\text{obj}}}{p_{\text{obj}}-p_{\text{scat}}}\right)^2 \sigma_{I_{\max}}^2. \tag{39}$$

It is obvious that if $p_{\text{obj}} \approx p_{\text{scat}}$, then $\{\sigma_{\hat{S}},\ \sigma_{\hat{B}}\} \to \infty$, hence the reconstruction is unstable. Thus, the method works best if the medium and object differ significantly in their DOPs. Specifically, in a medium where p_{scat} is relatively high (usually in good visibility), the method works best with depolarizing objects. On the other hand, in a strongly depolarizing medium (low p_{scat}), objects are reconstructed better if they are polarizing. Note that in Eqs. (38,39), the noise component due to $I_{\min}$ is amplified more than that of $I_{\max}$. For example, consider $\sigma_{\hat{S}}^2$. If $p_{\text{scat}} = 0.5$, then $\sigma_{I_{\min}}^2$ is amplified 9 times more than $\sigma_{I_{\max}}^2$.

Let us look for a moment on a case where signal-independent noise dominates. Then, $\sigma_{I_{\max}} = \sigma_{I_{\min}} = \sigma_0$, and

$$\sigma_{\hat{S}}^2 = 2\sigma_0^2\left[\frac{1+p_{\text{scat}}^2}{(p_{\text{obj}}-p_{\text{scat}})^2}\right],\quad \sigma_{\hat{B}}^2 = 2\sigma_0^2\left[\frac{1+p_{\text{obj}}^2}{(p_{\text{obj}}-p_{\text{scat}})^2}\right]. \tag{40}$$

Fig. 17 depicts $\sigma_{\hat{S}}/\sigma_0$ and $\sigma_{\hat{B}}/\sigma_0$, as derived in Eq. (40). The cases $[p_{\text{scat}},\ p_{\text{obj}}] = [0,1]$ and $[p_{\text{scat}},\ p_{\text{obj}}] = [1,0]$ are two local minima. In other words, it is preferable that polarization of either the backscatter or the backreflection would be high and exclusive. In any case, $\{\sigma_{\hat{B}},\ \sigma_{\hat{S}}\} > 1$, i.e., the noise is amplified.

In reality, $\sigma_{I_{\max}} \neq \sigma_{I_{\min}}$ due to photon noise. Define g_{electr} as the number of photo-generated electrons required to change a unit gray-level. Following [34], [42], the noise variance of a pixel gray level in an image I can be modeled as:

$$\sigma_I^2 = \rho^2/g_{\text{electr}}^2 + Dt/g_{\text{electr}}^2 + \frac{I(\mathbf{x}_{\text{obj}})}{g_{\text{electr}}}, \tag{41}$$

where ρ is the standard deviation (STD) of the electronic readout noise, induced by electronic circuity in the camera system. It is

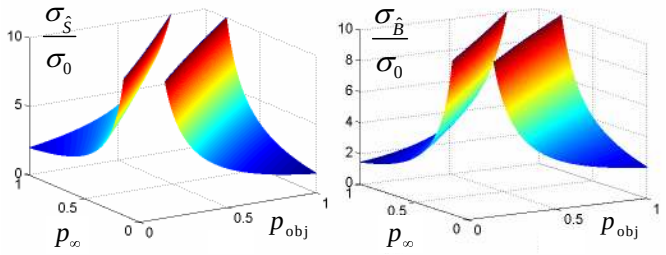

Fig. 17. The noise standard deviations $\sigma_{\hat{B}}$ and $\sigma_{\hat{S}}$ as a function of σ_0, p_{obj} and p_{scat}. The diagonal $p_{\text{obj}} = p_{\text{scat}}$ is unstable and therefore it is cut from the illustration.

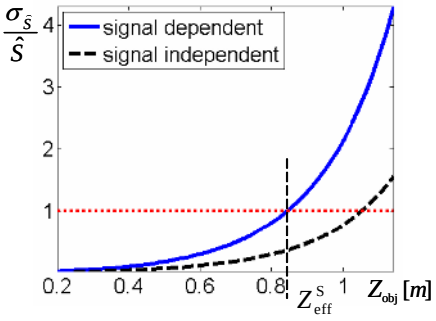

Fig. 18. STD of the reconstruction noise of $\hat{S}$, as a function of Z_{obj}. The effective distance Z_{eff}^S is defined as the distance, beyond which the noise STD in $\hat{S}$ is greater than $\hat{S}$ itself. In this case, it is in the order of a meter.

measured as a number e^- of electrons. Here, t is the exposure time, while D is the detector dark current in units of e^-/sec. In Eq. (41), the first two terms are *signal-independent*. The third term is photon noise, which is *signal-dependent*. As in [42], the signal independent components are encompassed into a single term

$$\kappa_{\text{gray}}^2 = \rho^2/g_{\text{electr}}^2 + Dt/g_{\text{electr}}^2, \tag{42}$$

assuming the same exposure time for all frames. Plugging Eqs. (41,42) into Eq. (38,39) yields

$$\sigma_{\hat{S}}^2(\mathbf{x}_{\text{obj}}) = \left(\frac{1+p_{\text{scat}}}{p_{\text{obj}}-p_{\text{scat}}}\right)^2\left[\kappa_{\text{gray}}^2 + \frac{I_{\min}(\mathbf{x}_{\text{obj}})}{g_{\text{electr}}}\right] + \left(\frac{1-p_{\text{scat}}}{p_{\text{obj}}-p_{\text{scat}}}\right)^2\left[\kappa_{\text{gray}}^2 + \frac{I_{\max}(\mathbf{x}_{\text{obj}})}{g_{\text{electr}}}\right] \tag{43}$$

$$\sigma_{\hat{B}}^2(\mathbf{x}_{\text{obj}}) = \left(\frac{1+p_{\text{obj}}}{p_{\text{obj}}-p_{\text{scat}}}\right)^2\left[\kappa_{\text{gray}}^2 + \frac{I_{\min}(\mathbf{x}_{\text{obj}})}{g_{\text{electr}}}\right] + \left(\frac{1-p_{\text{obj}}}{p_{\text{obj}}-p_{\text{scat}}}\right)^2\left[\kappa_{\text{gray}}^2 + \frac{I_{\max}(\mathbf{x}_{\text{obj}})}{g_{\text{electr}}}\right]. \tag{44}$$

Let us look at the case where $p_{\text{obj}} = 0$. From Eq. (16), Eq. (43) then becomes

$$\sigma_{\hat{S}}^2(\mathbf{x}_{\text{obj}}) = \frac{1}{p_{\text{scat}}^2}\cdot \left\{\left[2\kappa_{\text{gray}}^2 + \frac{S(\mathbf{x}_{\text{obj}})}{g_{\text{electr}}}\right](1+p_{\text{scat}}^2) + \frac{B(\mathbf{x}_{\text{obj}})}{g_{\text{electr}}}(1-p_{\text{scat}}^2)\right\}. \tag{45}$$

Interestingly, $\sigma_{\hat{S}}^2$ increases with the backscatter component $\mathbf{B}$. Therefore, it is beneficial to reduce $\mathbf{B}$ during acquisition. We can

further use Eqs. (5,21,45) to approximate[7] the dependency of $\sigma_{\hat{S}}$ on $Z_{\rm obj}$:

$$\sigma^2_{\hat{S}}(\mathbf{x}_{\rm obj}) = \frac{1}{p^2_{\rm scat}} \cdot \left\{ \frac{B_\infty\{1-\exp[-k(Z_{\rm obj}-Z_0)]\}}{g_{\rm electr}}(1-p^2_{\rm scat}) + \left[2\kappa^2_{\rm gray} + \frac{L_{\rm obj}(\mathbf{x}_{\rm obj})\exp[-2cZ_{\rm obj}]}{g_{\rm electr}Z^2_{\rm obj}}\right](1+p^2_{\rm scat})\right\}. \quad (46)$$

We define the *effective reconstruction distance* $Z^S_{\rm eff}$ as the distance for which:

$$\frac{\sigma_{\hat{S}}(Z^S_{\rm eff})}{\hat{S}(Z^S_{\rm eff})} \approx 1. \quad (47)$$

This is the distance, beyond which the noise STD in $\hat{S}$ is greater than $\hat{S}$ itself. Note that when the signal dependent component is negligible compared to $\kappa^2_{\rm gray}$, then Eq. (46) degenerates to Eq. (40), by substituting $\sigma_0 = \kappa_{\rm gray}$ and $p_{\rm obj} = 0$.

To gain insight into the dependency of $\sigma_{\hat{S}}$ on $Z_{\rm obj}$, we numerically assess two cases. The first takes into consideration only the signal-independent noise $\kappa_{\rm gray}$. The second case accounts for all noise effects (the model of Eq. 41). Let $B_\infty = 250$, i.e. close to saturation in an 8-bit camera. Assume a moderate[8] value for the DOP, $p_{\rm scat} = 0.6$ and attenuation coefficient $c = 0.2m^{-1}$. Furthermore, we set $Z_0 = 0.2m$, which is a typical value derived in simulations of setups where the light source is in proximity to the camera. For acquisition noise, we use typical values from [42]: $\kappa_{\rm gray} = 0.4$, $g_{\rm electr} = 50$. Based on these values we assess Eq. (46) with these values. The results are shown in Fig. 18. Clearly, when taking into consideration photon noise, $Z^S_{\rm eff}$ shortens. We note that we repeated this analysis for different setups of camera/light-source and types of water. Changing the setup hardly changes $Z^S_{\rm eff}$. However, increasing the visibility (decreasing c), increases $Z^S_{\rm eff}$ a little. In any case, $Z^S_{\rm eff}$ is in the order of a few meters. Apparently, this result does not fit our experiments, where we reconstructed objects up to $5-6m$. However, our simulation suggests that whereas the objects' visibility is enhanced by the reconstructions, the quantitative radiance values may be inaccurate.

B. Noise in $\hat{Z}_{\rm obj}$

In Sec. V-A the distance map $\hat{Z}_{\rm obj}$ is estimated based on $\hat{B}$. Here we analyze the effectiveness of the estimation. The noise in the estimated $\hat{\mathbf{B}}$ is uncorrelated with the noise in $\mathbf{B}_\infty$, as both are based on different measurements. Therefore, in analogy to Eq. (37), the noise variance in the estimated distance is

$$\sigma^2_{\hat{Z}_{\rm obj}} = \left(\frac{\partial \hat{Z}_{\rm obj}}{\partial \hat{B}}\right)^2 \sigma^2_{\hat{B}} + \left(\frac{\partial \hat{Z}_{\rm obj}}{\partial B_\infty}\right)^2 \sigma^2_{B_\infty}, \quad (48)$$

in first order approximation. The value of B_∞ does not change between frames. Thus it can be calibrated accurately once, setting $\sigma^2_{B_\infty} \simeq 0$. From Eq. (22):

$$\frac{\partial \hat{Z}_{\rm obj}}{\partial \hat{B}} = \left[\frac{1}{k(1-B_{\rm rel})}\right]\frac{1}{B_\infty}. \quad (49)$$

Hence,

$$\sigma^2_{\hat{Z}_{\rm obj}} = \left[\frac{1}{k(1-B_{\rm rel})B_\infty}\right]^2 \sigma^2_{\hat{B}} = \frac{\exp[2k(Z_{\rm obj}-Z_0)]}{k^2 B^2_\infty}\sigma^2_{\hat{B}}, \quad (50)$$

where $\sigma^2_{\hat{B}}$ is given by Eq. (44). As expected, $\sigma_{\hat{Z}_{\rm obj}} \to \infty$, i.e., the noise is greatly amplified as $B_{\rm rel} \to 1$, i.e. when $Z_{\rm obj} \gg Z_0$, destabilizing the reconstruction. However, this exponential amplification breaks the first-order approximation in Eqs. (37,48). Thus, Eq. (50) is valid only at small values of $Z_{\rm obj}$. Beyond that range, the effect of noise cannot be based on Eq. (48), and it is thus assessed numerically. When $Z_{\rm obj}$ increases, some noisy pixels yield $\hat{B} \geq B_\infty$, contradicting the physical model. Then, $\hat{B}_{\rm rel} \geq 1$ and the argument of the logarithm in Eq. (22) is either 0 or negative. This yields values of $\hat{Z}_{\rm obj}$ that are not physical (complex values). Having even a single pixel of such nature invalidates the variance calculation, and therefore $\sigma_{\hat{Z}_{\rm obj}}$ is undefined in that range.

To assess the effect of noise with respect to ground truth data, we performed numerical simulations. We simulated the acquisition process described in Sec. IV using the model from Sec. II. Noise was added to the simulated images to obtain $I_{\rm min}$ and $I_{\rm max}$. Then, the distance $\hat{Z}_{\rm obj}$ (which is now noisy) is reconstructed from $I_{\rm min}$ and $I_{\rm max}$ using Eqs. (13,22). We used the same parameters as in Sec. VII-A, $I_{\rm max}, I_{\rm min} \in [0, 255]$, and $p_{\rm obj} = 0$. Fig. 19(a) plots $\sigma_{\hat{Z}_{\rm obj}}/Z_{\rm obj}$ in the range $Z_{\rm obj} = [0, 1]m$. The solid line shows the empirical noise variance obtained in the numerical simulation. At small values of $Z_{\rm obj}$, it is consistent with the first-order theoretical approximation (Eq. 50), which is plotted as a dashed curve. When $Z_{\rm obj}$ increases, the actual noise grows beyond the first-order calculation.

As written above, at large distances the empirical $\sigma_{\hat{Z}_{\rm obj}}$ is undefined. Thus, in large distances, we assess the effect of noise using other measures. Let us define Ω_z as the set of all physically valid pixels located in the same distance z:

$$\Omega_z = \{\mathbf{x} : \quad \hat{B}_{\rm rel}(\mathbf{x}) < 1 \ , \ Z_{\rm obj}(\mathbf{x}) = z\}. \quad (51)$$

The average estimated distance in the set Ω_z is

$$\bar{Z}_{\rm obj}(z) = \frac{1}{|\Omega_z|}\sum_{\mathbf{x}\in\Omega_z} \hat{Z}_{\rm obj}(\mathbf{x}). \quad (52)$$

The average $\bar{Z}_{\rm obj}(z)$ is regarded as the expected distance reconstruction for pixels corresponding to distance $Z_{\rm obj} = z$. We estimated $\bar{Z}_{\rm obj}(z)$ in the simulation whose parameters are described above. For this case, Fig. 19(b) plots $\bar{Z}_{\rm obj}(z)$ as a function of $Z_{\rm obj}$. The distance estimation is in agreement with the ground truth up to a distance of $\sim 1[m]$. At some point, $\bar{Z}_{\rm obj}$ effectively does not change with $Z_{\rm obj}$. We term the distance where it happens $Z^{Z_{\rm obj}}_{\rm eff}$, beyond which the distance estimation becomes meaningless. This short range can be observed in Fig. 9. The bucket in the middle of the scene is placed in $Z_{\rm obj} \approx 2m$. As expected, the value of $B_{\rm rel}$ at the bucket is saturated, and thus the bucket appears as having the same distance as the background. Fig. 19(c) plots $1 - |\Omega_z|/N_z$, where N_z is total number of pixels (both valid and invalid) corresponding to the true distance z. This is the percentage of the physically invalid pixels, i.e., where $\hat{B}_{\rm rel} \geq 1$. Above $Z_{\rm obj} \approx 1[m]$ this percentage increases rapidly, which is in agreement with the loss of accuracy shown in Fig. 19(b).

[7] For the falloff calculation in Eq. (46), we assumed the simple case of collinearity of the camera and the light source axis. Eq. (46) also assumes a uniform light source.

[8] This DOP value was chosen following our experiments, described in Sec. IV-B.

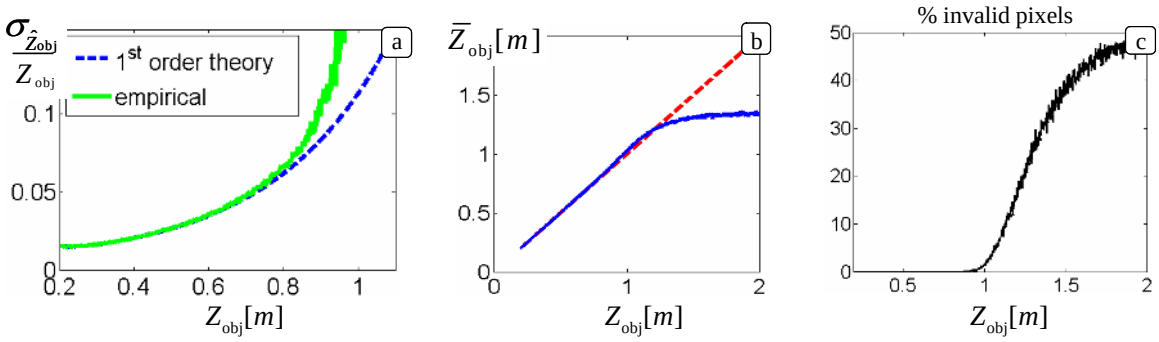

Fig. 19. (a) The value of $\sigma_{\hat{Z}_{\rm obj}}/Z_{\rm obj}$ in the range $Z_{\rm obj}=[0,1]$: theoretical first order [dashed] and empirical [solid]. (b) The expected distance reconstruction $\bar{Z}_{\rm obj}(z)$ [solid] based on valid pixels, in comparison to the utopian output $Z_{\rm obj}$ [dashed]. (c) Percentage of the invalid pixels $(1-|\Omega_z|/N_z)$ as a function of $Z_{\rm obj}$. In these pixels $\hat{B}_{\rm rel}\geq 1$.

VIII. Summary

We presented a polarization-based method for visibility enhancement and distance estimation in scattering media. The method was demonstrated in real-life experiments. Our method uses two frames taken with widefield polarized illumination. Therefore, it is fast and simple. We use wide band light sources, enabling colorful results. The visibility enhancement range depends on the range of the light source. However, underwater, the distance reconstruction is effective only in a range of $1-2m$. In the future, it would be beneficial to expand the work to deal with objects whose reflectance has spatially varying $p_{\rm obj}$. While we performed experiments in the underwater domain, the formulation of most of our problems is general and may thus be applicable to other media. This work can be incorporated together with other methods for vision in scattering media [12].

The analysis in this paper used the single scattering approximation. In principle, multiple scattering may occur. At least in one of our experiments (sea of Galillee, Fig. 7(a)), multiple scattering was significant, creating noticeable blur. Our method still resulted in visibility enhancement. Nevertheless, it will be beneficial to analyze the effects caused by multiple scattering on the methods we presented in this paper.

Appendix

At the current stage of the research, we wanted to reduce effects that can potentially disturb the experimental demonstration. Hence, we had several consideration for choosing the light sources, beyond being watertight in the underwater depth.

- **Stability**: We had to avoid uncontrolled illumination fluctuations in this research phase. Hence, we avoided current arc-based flash bulbs, which have $\mathcal{O}(5\%)$ fluctuations [13]. DC incandescent sources are least prone to short-term fluctuations, once their temperature saturates.
- **Narrow lamphead exit aperture** enables fitting of high quality filters. Hence, we avoided current large LED clusters or fluorescent bulbs.
- **Holographic diffusers** are used for higher transmission efficiency and smaller diffusing angles than ground glass diffusers.
- **Sealed diffuser**. High efficiency diffusers are either ground/sandblusted glass or holographic. The former become clear (nondiffusing) in water, as their refractive index is nearly matched by water in their concavities. The latter are destroyed in water. Thus, we sealed the diffusers in air spaced windows.
- **Diffuser before polarizer**. Diffusers scramble light, causing depolarization. Lab tests verified a higher illumination DOP when the diffuser is placed between the polarizer and the lamphead, rather than facing the object.
- **High intensity** extends the vision range in the water.
- **Enough battery power** to last for long underwater experiments with fast recharging in field use.

We used the Aquavideo SuperNova system. It projects up to 400W by two incandescent bulbs. A lower power of 80W lasts for about an hour. It has a 50mm lamphead exit. The above considerations stemmed from research needs. In a system for routine use, part of these considerations may be relaxed.

Acknowledgements

We thank Dori Yelin, Haim Kermany, Ben Herzberg and above all Einav Namer for help in the experimental dives. We thank Nadav Shashar for fruitful discussions and great help. Yoav Schechner is a Landau Fellow - supported by the Taub Foundation, and an Alon Fellow. The work was supported by the Israeli Science Foundation (grant No. 315/04) and by the Ollendorff Center in the Elect. Eng. Dept. at the Technion. Minerva is funded through the BMBF.

References

[1] P. Barham, L. Andreone, X. H. Zhang, and M. Vaché. The development of a driver vision support system using far infrared technology: progress to date on the darwin project. In *Proc. IEEE Int. Vehicle Sympos.*, pages 545–549, 2000.

[2] M. Ben-Ezra. Segmentation with invisible keying signal. In *Proc. IEEE CVPR*, volume 1, pages 32–37, 2000.

[3] T. Chen, H. P. A. Lensch, C. Fuchs, and H. P. Seidel. Polarization and phase-shifting for 3D scanning of translucent objects. In *Proc. IEEE CVPR*, 2007.

[4] F. Cozman and E. Kroktov. Depth from scattering. In *Proc. IEEE CVPR*, pages 801–806, 1997.

[5] O. G. Cula, K. J. Dana, D. K. Pai, and D. Wang. Polarization multiplexing for bidirectional imaging. In *Proc. IEEE CVPR*, volume 2, pages 1116–1123, 2005.

[6] S. G. Demos and R. R. Alfano. Temporal gating in highly scattering media by the degree of optical polarization. *Opt. Lett.*, 21:161–163, 1996.

[7] Y. Diamant and Y. Y. Schechner. Overcoming visual reverberations. *Accepted to IEEE CVPR*, 2008.

[8] H. Farid and E. H. Adelson. Separating reflections from images by use of independent component analysis. *J. Opt. Soc. Amer. A*, 16:2136–2145, 1999.

[9] G. R. Fournier, D. Bonnier, L. J. Forand, and P. W. Pace. Range-gated underwater laser imaging system. *Opt. Eng*, 32:2185–2190, 1993.

[10] G. C. Giakos. Active backscattered optical polarimetric imaging of scattered targets. In *IEEE Instr. & Measurement Tech. Conf.*, volume 1, pages 430–432, 2004.

[11] G. D. Gilbert and J. C. Pernicka. Improvement of underwater visibility by reduction of backscatter with a circular polarization technique. *App. Opt.*, 6:741–746, 1967.

[12] M. Gupta, S. Narasimhan, and Y. Y. Schechner. On controlling light transport in poor visibility environments. *Accepted to IEEE CVPR*, 2008.

[13] Hamamatsu. Xenon flash lamps. Catalog TLSX1008E04 (Hamamatsu Photnics K.K., Electron Tube Center), 1998.

[14] S. Harsdorf, R. Reuter, and S. Tönebön. Contrast-enhanced optical imaging of submersible targets. In *Proc. SPIE*, volume 3821, pages 378–383, 1999.

[15] E. S. Harvey and M. R. Shortis. Calibration stability of an underwater stereo-video system: Implications for measurement accuracy and precision. *Marine Technology Society (MTS) Journal*, 32(2):3–17, 1998.

[16] S. L. Jacques, J.C. Ramella-Roman, and K. Lee. Imaging skin pathology with polarized light. *J. of Biomed. Opt.*, 7:329–340, 2002.

[17] J. S. Jaffe. Computer modelling and the design of optimal underwater imaging systems. *IEEE J. Oceanic Eng.*, 15:101–111, 1990.

[18] W. S. Jagger and W. R. A. Muntz. Aquatic vision and the modulation transfer properties of unlighted and diffusely lighted natural waters. *Vis. Res.*, 33:1755–1763, 1993.

[19] G. Jarry, E. Steimer, V. Damaschini, M. Epifanie, M. Jurczak, and R. Kaiser. Coherence and polarization of light propagating through scattering media and biological tissues. *App. Opt.*, 37:7357–7367, 1998.

[20] R. Kaftory, Y. Y. Schechner, and Y. Y. Zeevi. Variational distance-dependent image restoration. In *Proc. IEEE CVPR*, pages 1–8, 2007.

[21] D. M. Kocak and F. M. Caimi. The current art of underwater imaging with a glimpse of the past. *Marine Technology Society (MTS) Journal*, 39:5–26, 2005.

[22] A. A. Kokhanovsky. *Light Scattering Media Optics*, page 200. Springer, 3rd edition, 2004.

[23] M. Levoy, B. Chen, V. Vaish, M. Horowitz, I. McDowall, and M. Bolas. Synthetic aperture confocal imaging. *ACM TOG*, 23:825–834, 2004.

[24] G. D. Lewis, D. L. Jordan, and P. J. Roberts. Backscattering target detection in a turbid medium by polarization discrimination. *App. Opt.*, 38:3937–3944, 1999.

[25] F. C. MacKintosh, J. X. Zhu, D. J. Pine, and D. A. Weitz. Polarization memory of multiply scattered light. *Phys. Rev. B 40*, 13:9342–9345, 1989.

[26] B. L. McGlamery. A computer model for underwater camera system. In *Proc. SPIE*, volume 208, pages 221–231, 1979.

[27] D. Miyazaki and K. Ikeuchi. Inverse polarization raytracing: estimating surface shape of transparent objects. In *Proc. IEEE CVPR*, volume 2, pages 910–917, 2005.

[28] C. D. Mobley. *Light and Water: Radiative Transfer in Natural Waters*, chapter 3,5. San-Diego: Academic Press, 1994.

[29] S. P. Morgan and M. E. Ridgway. Polarization properties of light backscattered from a two layer scattering medium. *Optics Express*, 7:395–402, 2000.

[30] S. G. Narasimhan and S. K. Nayar. Vision and the atmosphere. *Int. J. Comp. Vision*, 48:233–254, 2002.

[31] S. G. Narasimhan, S. K. Nayar, B. Sun, and S. J. Koppal. Structured light in scattering media. In *Proc. IEEE ICCV*, volume 1, pages 420–427, 2005.

[32] S. K. Nayar, G. Krishnan, M. D. Grossberg, and R. Raskar. Fast separation of direct and global components of a scene using high frequency illumination. In *ACM SIGGRAPH*, pages 935–944, 2006.

[33] M. J. Rakovic, G. W. Kattawar, M. Mehrubeoglu, B. D. Cameron, L. V. Wang, S. Rastegar, and G. L. Coté. Light backscattering polarization patterns from turbid media: theory and experiment. *App. Opt.*, 38:3399–3408, 1999.

[34] N. Ratner and Y. Y. Schechner. Illumination multiplexing within fundamental limits. In *Proc. IEEE CVPR*, pages 1–8, 2007.

[35] V. Sankaran, M. J. Everett, D. J. Maitland, and J. T. Walsh Jr. Comparison of polarized-light propagation in biological tissue and phantoms. *Opt. Lett.*, 24:1044–1046, 1999.

[36] V. Sankaran, J. T. Walsh, and D. J. Maitland. Comparative study of polarized light propagation in biologic tissues. *J. Biomed. Opt.*, 7:300–306, 2002.

[37] Y. Y. Schechner and Y. Averbuch. Regularized image recovery in scattering media. *IEEE Trans. PAMI*, 29(9):1655–1660, 2007.

[38] Y. Y. Schechner and N. Karpel. Clear underwater vision. In *Proc. IEEE CVPR*, volume 1, pages 536–543, 2004.

[39] Y. Y. Schechner and N. Karpel. Recovery of underwater visibility and structure by polarization analysis. *IEEE J. Oceanic Eng.*, 30:570–587, 2005.

[40] Y. Y. Schechner, S. G. Narasimhan, and S. K. Nayar. Instant dehazing of images using polarization. In *Proc. IEEE CVPR*, volume 1, pages 325–332, 2001.

[41] Y. Y. Schechner, S. G. Narasimhan, and S. K. Nayar. Polarization-based vision through haze. *App. Opt.*, 42:511–525, 2003.

[42] Y. Y. Schechner, S. K. Nayar, and P. N. Belhumeur. Multiplexing for optimal lighting. *IEEE Trans. PAMI*, 29(8):1339–1354, 2007.

[43] Y. Y. Schechner, J. Shamir, and N. Kiryati. Polarization and statistical analysis of scenes containing a semi-reflector. *J. Opt. Soc. Amer. A*, 17:276–284, 2000.

[44] N. Shashar, S. Sabbah, and T. W. Cronin. Transmission of linearly polarized light in seawater: implications for polarization signaling. *J. Experimental Biology*, 207:3619–3628, 2004.

[45] S. Shwartz, E. Namer, and Y. Y. Schechner. Blind haze separation. In *Proc. IEEE CVPR*, volume II, pages 1984–1991, 2006.

[46] S. Shwartz, M. Zibulevsky, and Y. Y. Schechner. Fast kernel entropy estimation and optimization. *Signal Processing*, 85(5):1045–1058, 2005.

[47] M. P. Strand. Imaging model for underwater range-gated imaging systems. In *Proc. SPIE*, volume 1537, pages 151–160, 1991.

[48] B. Sun, R. Ramamoorthi, SG. Narasimhan, and SK Nayar. A practical analytic single scattering model for real time rendering. *ACM TOG*, 24:1040–1049, 2005.

[49] B. A. Swartz and J. D. Cummings. Laser range-gated underwater imaging including polarization discrimination. In *Proc. SPIE.*, volume 1537, pages 42–56, 1991.

[50] T. Treibitz and Y. Y. Schechner. Instant *3*Descatter. In *Proc. IEEE CVPR*, pages 1861–1868, 2006.

[51] T. Treibitz, Y. Y. Schechner, and H. Singh. Flat refractive geometry. *Accepted to IEEE CVPR*, 2008.

[52] J. S. Tyo, M. P. Rowe, E. N. Pugh, and N. Engheta. Target detection in optically scattering media by polarization-difference imaging. *App. Opt.*, 35:1855–1870, 1996.

[53] B. Wells. MTF provides an image-quality metric. *Laser Focus World*, 41(10), 2005.

[54] L. B. Wolff. Polarization vision: a new sensory approach to image understanding. *Image & Vision Comp.*, 15:81–93, 1997.

Tali Treibitz Tali Treibitz received her BA degree in computer science from the Technion-Israel Institute of Technology in 2001. She is currently a Ph.D. candidate in the department of Electrical Engineering, Technion. Her research involves physics-based computer vision. She is also an active PADI open water scuba instructor.

Yoav Y. Schechner Yoav Y. Schechner received his BA and MSc degrees in physics and PhD in electrical engineering from the Technion-Israel Institute of Technology in 1990,1996, and 2000, respectively. During the years 2000 to 2002 Yoav was a research scientist at the computer science department in Columbia University. Since 2002, he is a faculty member at the department of Electrical Engineering of the Technion, where he heads the Hybrid Imaging Lab. His research is focused on computer vision, the use of optics and physics in imaging and computer vision, and on multi-modal sensing. He was the recipient of the Wolf Foundation Award for Graduate Students in 1994, the Guttwirth Special Distinction Fellowship in 1995, the Ollendorff Award in 1998 and the Morin Fellowship in 2000- 2002. He is now a Landau Fellow - supported by the Taub Foundation. He has received the Klein Research Award in 2006 and the Outstanding Reviewer Awards in IEEE CVPR 2007 and ICCV 2007.